The fracture toughness of polysilicon microdevices: A first report

R. Ballarini, R. L. Mullen, and Y. Yin
Department of Civil Engineering, Case Western Reserve University, Cleveland, Ohio 44106-7201

H. Kahn, S. Stemmer, and A. H. Heuer
Department of Materials Science and Engineering, Case Western Reserve University, Cleveland, Ohio 44106-7204

Polysilicon microfracture specimens were fabricated using surface micromachining techniques identical to those used to fabricate microelectromechanical systems (MEMS) devices. The nominal critical J-integral (the critical energy release rate) for crack initiation, J_c, was determined in specimens whose characteristic dimensions were of the same order of magnitude as the grain size of the polysilicon. J_c values ranged from 16 to 62 N/m, approximately a factor of four larger than J_c values reported for single crystal silicon.

I. INTRODUCTION

Significant research has been conducted on the development of designs, modeling, and production processes for microelectromechanical systems (MEMS) devices. However, long-term durability of various MEMS devices, which requires a fundamental understanding of the fatigue and fracture characteristics of such microfabricated structures (known as "microstructures" in MEMS jargon), has not been fully addressed in a systematic fashion. While there is a significant technology base in the wear, fatigue, and fracture of macro systems, the study of fatigue and fracture on the microscale appropriate for MEMS is very limited. Furthermore, the fracture mechanics base for polysilicon, one of the principal materials currently used in the fabrication of MEMS devices, is sparse at best. The determination of mechanical properties at the scale relevant to MEMS devices is complicated by the anisotropy and heterogeneity inherent in the microfabricated structures, the residual stresses resulting from processing, and the resulting batch-to-batch statistical variations. To our knowledge, the only existing experimental fracture mechanics study at the microscale was conducted by Connally and Brown[1] on single crystal silicon, and by Fan, Howe, and Muller[2] on CVD-formed silicon nitride and low-stress silicon nitride.

Connally and Brown's goal was to determine whether silicon is prone to static fatigue. By using a bulk micromachined cantilever specimen whose natural frequency is sensitive to small changes in the length of the precrack, they were able to show that in humid air, crack growth does occur, albeit at a relatively slow rate. Fan *et al.* estimated the fracture toughness, K_{Ic}, of low-stress silicon nitride as 1.8 ± 0.3 MPa $\sqrt{\mathrm{m}}$.

An understanding of the relationships between processing variables and the resulting mechanical behavior and durability of microfabricated structures is needed in order to allow rational design of MEMS devices. To quantify the statistical influence of various surface treatments on the stiffness and strength of *p*-doped single crystal silicon, Ericson and Schweitz[3] and Johansson, Ericson, and Schweitz[4] have conducted tests using cantilever beams that were fabricated by bulk micromachining of single crystal silicon wafers. These beams were not fracture mechanics specimens and therefore did not provide data which could be used to directly estimate fracture toughness. However, their results showed that the surface treatments can have a great influence on strength. For example, while diamond polishing significantly decreased strength, polishing followed by oxidation increased strength.

The present work involves study of the mechanical behavior, specifically the fracture characteristics, of relatively thick (up to 7.5 μm) polysilicon films fabricated using procedures identical to those used for current MEMS devices. We have developed a microfracture specimen whose characteristic dimensions, notch tip radius, and uncracked ligament length are comparable to the grain size of the polysilicon, and present data on the critical value of the nominal J-integral for fracture initiation, J_c. (The experimental program and resulting data discussed in this paper were introduced briefly in a summary paper dealing with mechanical properties of thick polysilicon films.[5]) Notwithstanding the inherent difficulties of microfracture mechanics experimentation, the values determined for J_c appear to be four times higher than those obtained using macro specimens of single crystal silicon. While the in-plane residual stresses which arise during both the film deposition process and the oxidation step involved in device fabrication are eliminated upon release of the structure from the substrate, some residual stresses due to gradients through the

film thickness may still exist. However, the difference we observe between single crystal and polycrystalline specimens is attributed mainly to stochastic fluctuations in the local resistance to crack initiation, due to microstructural heterogeneities and material anisotropies, whose importance is magnified in these microfracture specimens.

II. FABRICATION AND CHARACTERIZATION OF MICROFRACTURE SPECIMENS

A typical microfracture specimen is shown in Fig. 1(a). The specimen is essentially a deeply cracked, double cantilever beam (A), suspended from an anchor (B) through two thin beams (C).

Our initial goal was to load the specimen electrostatically through the comb actuators (D). It was estimated that a total force equal to 10 μN would be developed, which together with a deeply cracked configuration, would produce a nominal stress intensity factor equal to that of single-crystal silicon ($\sim$1 MPa$\sqrt{m}$). In fact, the generated force for this design was not sufficient to initiate crack propagation, and the fabricated specimens were loaded mechanically through a 10 μm diameter probe inserted along the crack surfaces, as will be explained subsequently.

The fracture devices were fabricated by standard surface micromachining techniques, using a single-mask process. First, wafers underwent a wet oxidation at 1100 °C for 14 h, to grow a 2.5 μm thick SiO$_2$ release layer, which is visible in Figs. 1(b) and 1(c). This was followed by the formation of the polysilicon films by chemical vapor deposition (CVD). The undoped films were grown at 610 °C at a total pressure of 244 mTorr, using SiH$_4$ gas; in all cases, a 2.5 or 5 μm thick film was formed in one run, and for thicker films, a second deposition was performed after exposure to the laboratory ambient. The boron-doped films were grown at 1100 °C, using a combination of SiCl$_3$H and B$_2$H$_6$ gases, following a brief nucleation step at 775 °C in SiH$_4$; the several thicknesses studied were each grown in a single deposition run, of course using different deposition times for the varying thicknesses. Because the surfaces of the as-deposited polysilicon films were very rough, some of the films were subjected to a chemo-mechanical polishing with a colloidal silica slurry (Syton), which converted the rough surface of the polysilicon films to a mirror finish. The polysilicon films were then oxidized to form a masking layer for a later polysilicon etch. This wet oxidation was carried out at 1000 °C, for 100 to 300 min, depending on the desired final-masking oxide thickness.

The micromechanical structures were patterned using standard optical lithography techniques. The masking oxide layer was dry etched in CHF$_3$, C$_2$F$_6$, and He,

flowing at 20, 8, and 45 sccm, respectively, at 2.4 Torr and 350 W rf, and an etch rate of 300 nm/min. The polysilicon etch recipe contains an initial native oxide removal step, to remove any SiO$_2$ on the surface. This etching was done for 40 s at 400 mTorr and 200 W, with SF$_6$, Cl$_2$, and He flow rates of 50, 80, and 120 sccm, respectively. The main portion of the etch was performed at 400 mTorr and 200 W, with Cl$_2$ and He flow rates of 80 and 120 sccm, respectively, using an optical endpoint detector. The etch rate was 400 nm/min, and a 1 min overetch was included. Both etch steps were done at an anode-to-wafer gap spacing of 6 mm. The selectivity was 24 : 1 with respect to SiO$_2$. This etching sequence is quite successful in achieving smooth, nearly vertical sidewalls in the thick polysilicon films.

The final step was to release the structures in hydrofluoric acid, which removed the release oxide, as well as any remnant masking oxide. This etching step was done for 10 min, so that some oxide remains beneath the larger features of the structures [B and D in Fig. 1(a)], leaving them anchored to the substrate, while the smaller features are fully released and free to move.

In both doped and undoped films, the individual grains have an average diameter of about 1 μm, as seen in the cross-sectional TEM images shown in Figs. 1(b) and 1(c) and the planar view micrograph of Fig. 1(d); it is clear that the microstructure of the fabricated devices is (nearly) columnar. This supports the plane strain finite element *J*-integral calibration of the specimen, which is presented in Sec. III.

Figure 1(b) shows the microstructure of a two-run film which exhibits a second "nucleation" layer of randomly oriented grains which formed at the beginning of the second run, most likely due to a thin native oxide on the surface of the first layer. The most striking feature of the microstructure is the density of vertically oriented {111} twin boundaries, which are known[6] to be the major intragranular defect in CVD-grown polysilicon. The columnar grains form by "evolutionary selection"[7] and result in an overall $\langle 110 \rangle$ texture, which was confirmed by x-ray pole figures (not shown here). The boron-doped films [Fig. 1(c)] were deposited at a higher temperature and exhibit a lower twin boundary density, but approximately the same average grain size as the undoped films [cf. Figs. 1(b) and 1(c)]. The lower twin boundary density in the doped films is thought to be due to the higher growth temperature.

Dislocations were also present in both the doped and undoped films, but the high density of twin boundaries prevented their systematic study. A HREM image of dislocations and twin boundaries in an undoped film is shown in Fig. 1(e). These dislocations may be associated with the residual compressive stresses present in as-deposited and oxidized films, which can be as high as 200 MPa.[5]
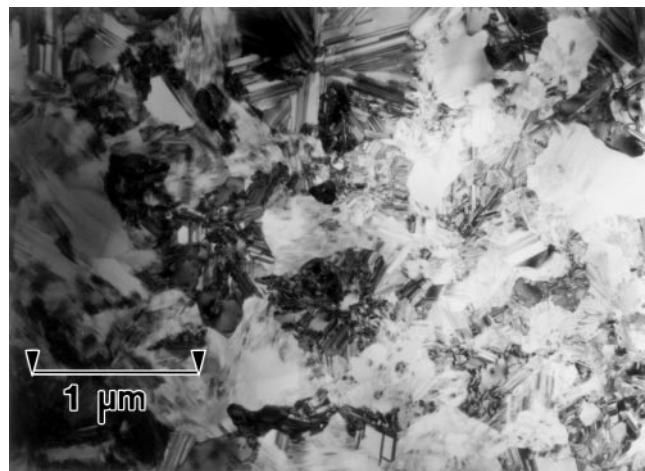
(a)

(b)

(c)
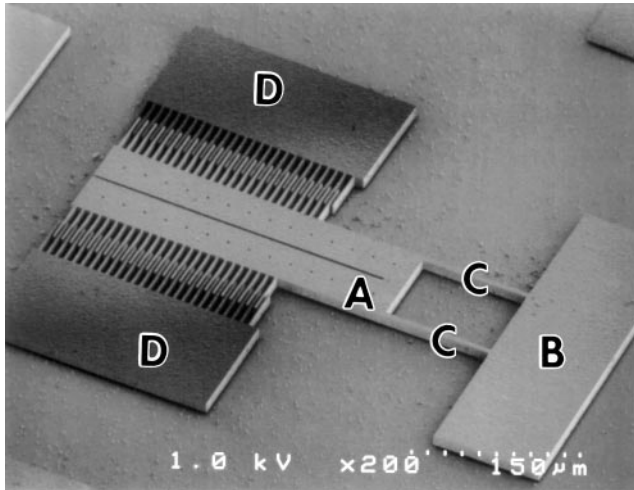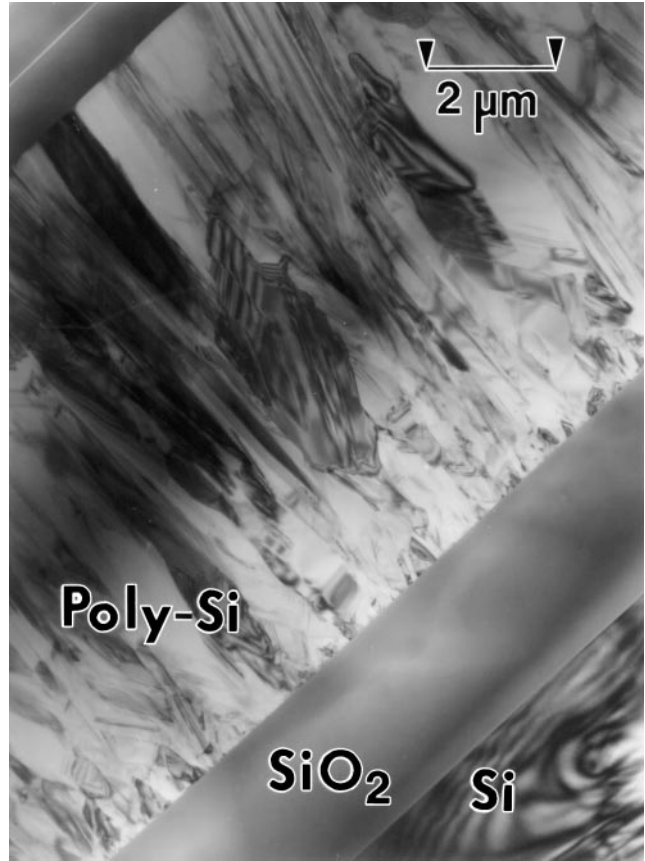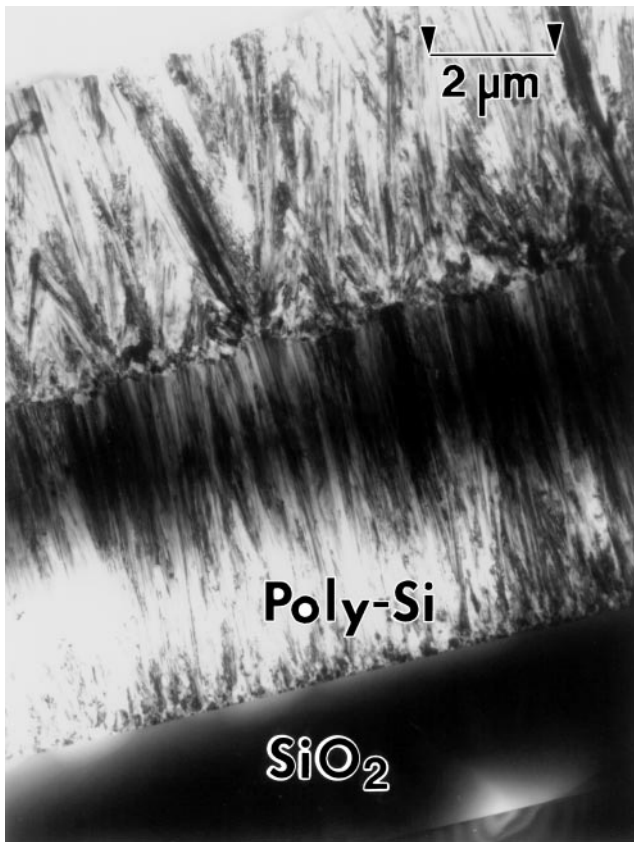
(d)

FIG. 1. Microstructure of polysilicon microfracture specimens: (a) shows a typical specimen, whose individual features (A–D) are described further in the text; (b) and (c) are cross-sectional transmission electron micrographs (TEM's) of undoped and B-doped CVD films, respectively; (d) shows a planar view micrograph of the grain and twin boundaries present in an as-fabricated undoped microdevice; and (e) shows a high resolution TEM image of dislocations (arrowed) and twin boundaries in an undoped sample. See text for further discussion.

III. ENERGY RELEASE RATE CALIBRATION PROCEDURE

A schematic drawing of the loaded fracture specimen is shown in Fig. 2(a), while the nominal dimensions are shown in Fig. 2(b). The thicknesses t of the specimen and the lengths x of the uncracked ligament were either 2.5, 5, 7.2, and 7.5 μm, and 6, 10, and 20 μm, respectively (see Table I). The comb free-travel distance a was either 8 or 18 μm. To cause failure of these
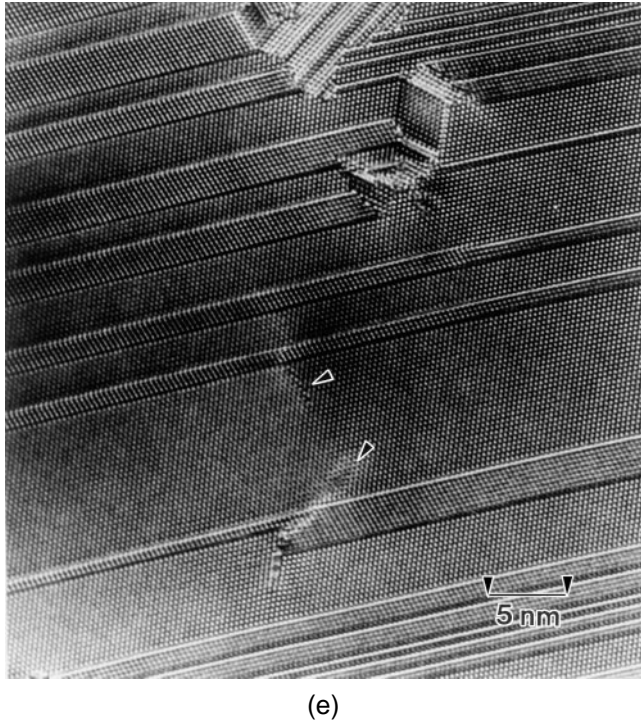
J. Mater. Res., Vol. 12, No. 4, Apr 1997

917

(e)

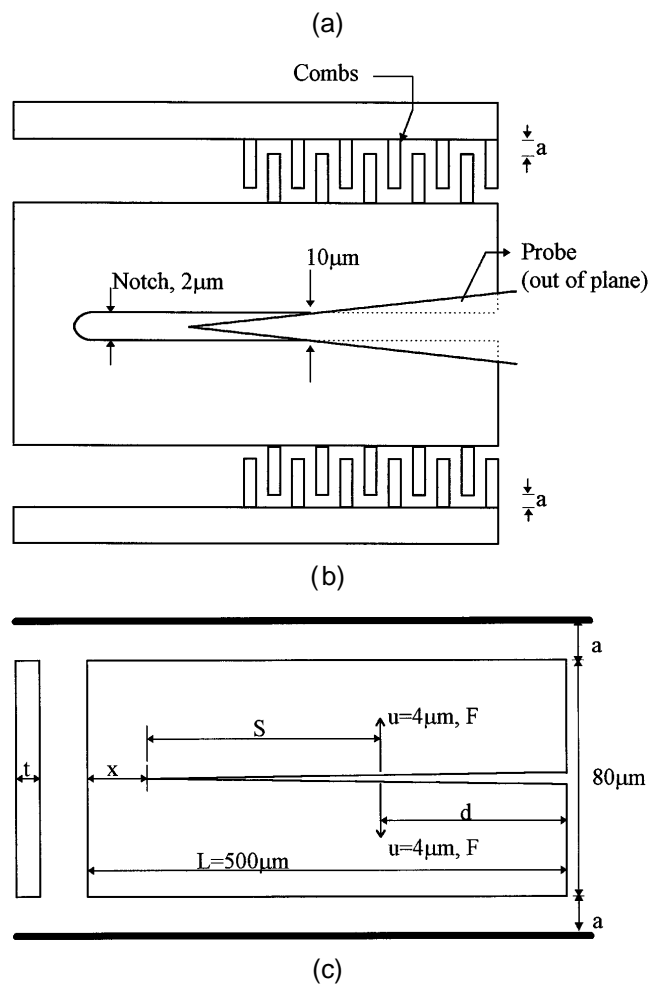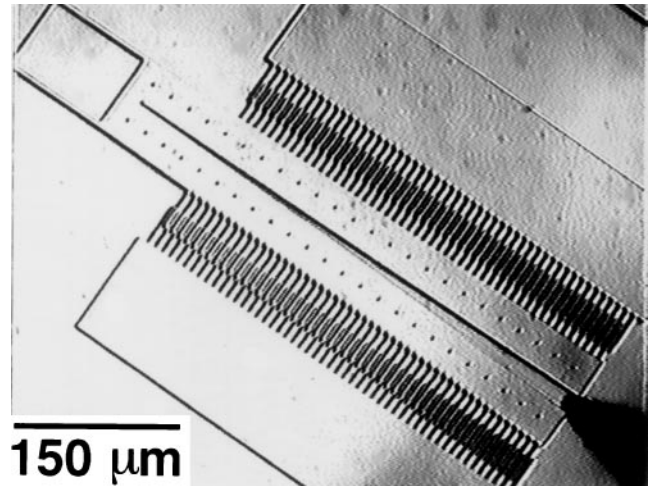FIG. 1. (*continued from previous page.*)

(a)

(b)

(c)

FIG. 2. (a) Micrograph of wedge loaded microfracture specimen; (b) schematic drawing of microfracture specimen; (c) variables and nominal dimensions used in the mathematical model.

microdevices, a rigid probe was used to wedge open the 2 μm wide notch, as shown in Fig. 2(a). The shaft of the tungsten carbide probe is 0.020″ in diameter and tapers to a conical point, with an inclusive angle of 15°, to a tip radius of 5 μm. As the probe was moved toward the crack tip, its position at crack initiation was observed and recorded on video. This information in turn was used to determine J_c, a fracture parameter appropriate for these specimens because the radius of the notch ($\sim$1 μm) is comparable to the average diameter of the grains ($\sim$1 μm). Furthermore, as will be discussed subsequently, even if the notch was a mathematically sharp crack, the region of dominance of the stress intensity factor is comparable to the average grain size for this deeply cracked configuration. For these reasons, the nominal stress intensity factor does not directly characterize the state of stress near the notch tip.

For computational convenience, the J-integral was calculated assuming the mathematically sharp crack, finite element model shown in Fig. 3(a). As will be discussed, the J-integral calculated using this model is practically the same as that associated with the rectangular blunt notch shown in Fig. 3(b). Because the loading is symmetric with respect to the traction-free crack line, only the top half of the specimen needs to be analyzed, as shown in these figures. The symmetry boundary conditions consistent with Mode I loading, namely zero displacement in the *y*-direction and zero force (shear stress) in the *x*-direction, were imposed

at all nodes ahead of the crack tip. These boundary conditions are represented by rollers A. The thin beams in Fig. 1(a) are represented by rollers B in Figs. 3(a) and

TABLE I. Critical energy release rate ($\overline{J}_c$) data.

Polysilicon				$\overline{J}_c$ (N/m)		
Thickness (μm)	Doped	Syton polished	Uncracked ligament length (μm)	Average	Standard deviation	Number of tests
2.5	Yes	Yes	6	134	48	5
2.5	Yes	Yes	10	126	27	6
2.5	Yes	Yes	20	747	412	6
5.0	Yes	Yes	6	53	22	7
5.0	Yes	Yes	10	62	20	8
5.0	Yes	Yes	20	58	8	6
7.5	Yes	Yes	6	38	16	5
7.5	Yes	Yes	10	19	4	6
7.5	Yes	Yes	20	16	8	5
5.0	No	No	6	26	4	4
5.0	No	No	10	24	8	4
5.0	No	No	20	28	14	6
7.2	No	Yes	6	25	11	3
7.2	No	Yes	10	24	4	3
7.2	No	Yes	20	26	6	4

3(b), which impose zero displacement in the *x*-direction, and unrestrained movement in the *y*-direction.

The *J*-integral for this specimen is calculated as follows. Young's modulus and Poisson's ratio are set equal to 160 GPa and 0.22, respectively. For the mathematically sharp crack, the opening displacement of the points along the surface of the crack that are in contact with the probe are prescribed as 4 μm. The solution provides the effective force per unit thickness *F*. A very fine mesh together with a rosette of singular elements was used to capture the square root stress singularity
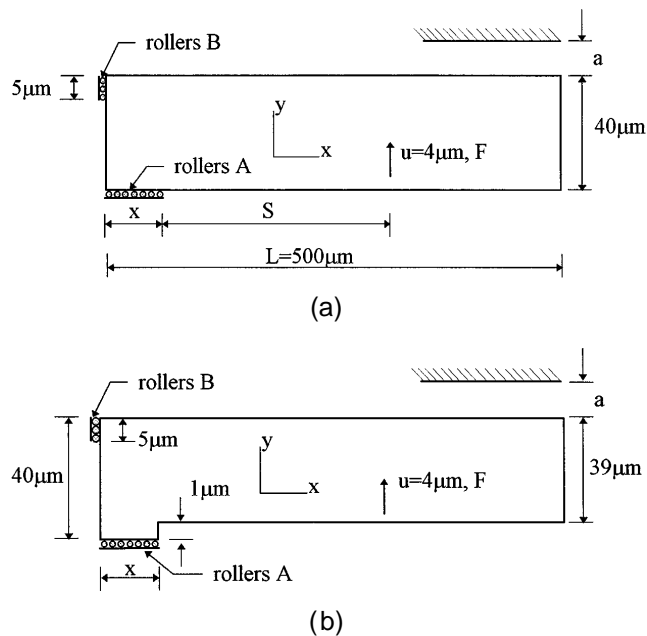
at the crack tip, and to calculate the stress intensity factor, K_I. The calculations considered the cases when the displacement of the points on the top surface of the specimen are equal to the free travel distance of the combs (distance *a* in Figs. 2 and 3).

The results of the calculations are shown in Figs. 4 and 5. For illustrative purposes, the case $a = \infty$ is presented in Figs. 4 and 5(a). Figure 4 shows the force per unit thickness for each value of uncracked ligament size. As the probe moves closer to the crack tip, the decreasing cantilever effect results in an increase in the force required to maintain the prescribed crack opening displacement. Concomitantly, the stress intensity factors follow the same trend, as shown in Fig. 5(a). The stress intensity factor corrections for several values of *a* are shown in Fig. 5(b) for $x = 6$ μm.
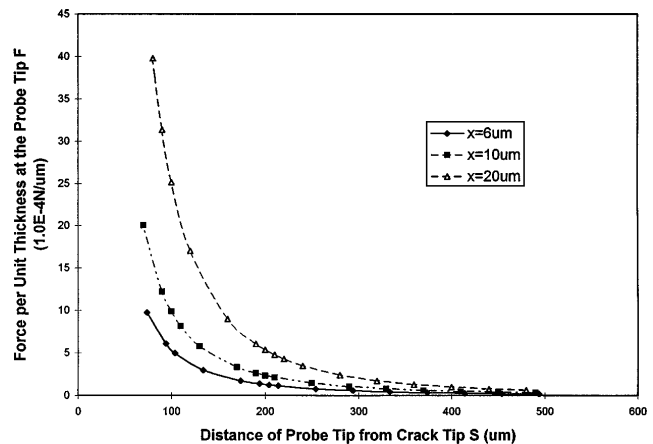

FIG. 3. Finite element models of microfracture specimen: (a) sharp crack, and (b) blunt rectangular notch.

FIG. 4. FEM calibration results showing the effective force versus probe position for the three ligament lengths.
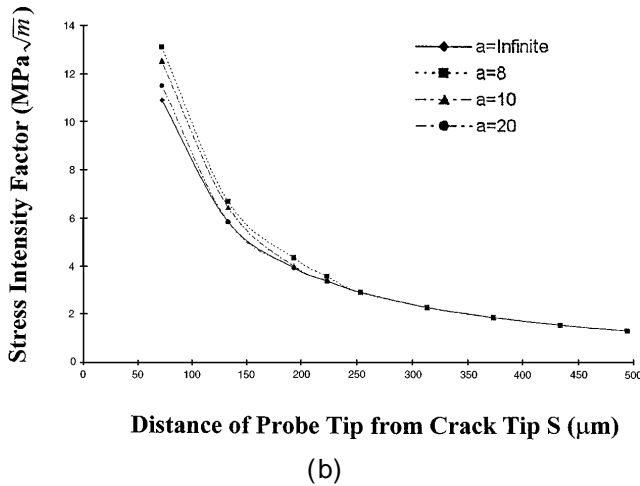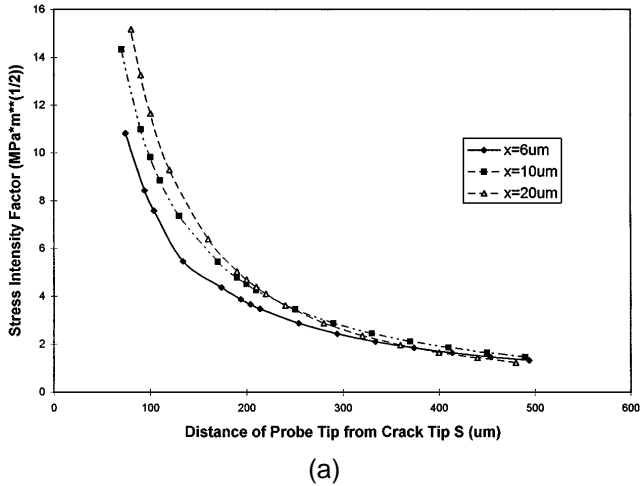
(a)

(b)

FIG. 5. (a) FEM calibration results showing the stress intensity factor versus probe position for the three ligament lengths; (b) typical FEM correction for free-travel distance of combs.

The classic (fixed end) double cantilever beam model was also used to approximate the stress intensity factor. The results, which are not presented here, are significantly different from those calculated using the finite element method, as the "trousers" of this specimen are considerably more compliant than a fixed beam.

Finally, the *J*-integral was derived from the numerically calculated stress intensity factor through the Irwin formula

$$J = \frac{(1 - \nu^2)K_I^2}{E}. \qquad (1)$$

Figure 6 shows a comparison between the *J*-integral calculated using Eq. (1) and that calculated using the blunt-notch configuration of Fig. 3(b). The latter was evaluated by estimating the change in potential energy associated with an infinitesimal self-similar advance of the notch tip. Neglecting the change in energy resulting
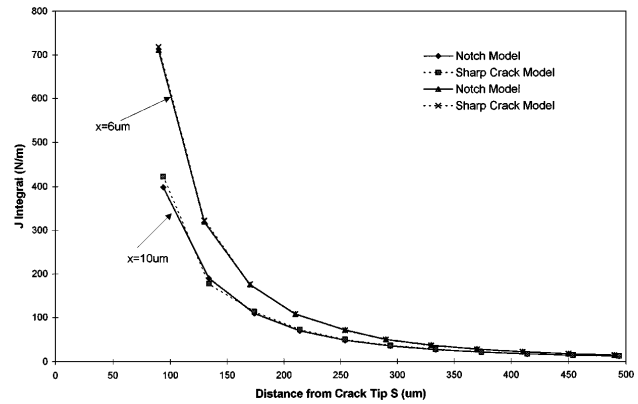

FIG. 6. Comparison of *J*-integral calibration for 6 and 10 μm ligament lengths for sharp cracks with blunt notches.

from removal of material, it is given by

$$J = -\frac{\partial \Pi}{\partial (L - x)} = \frac{\partial \Pi}{\partial x}, \qquad (2)$$

where Π is the potential energy per unit thickness. The sharp crack and the blunt notch produce practically the same results. The normal stresses ahead of the sharp crack are shown in Figs. 7(a)–7(c) for probe position $d = 290$ μm. In these plots the dashed line represents the finite element method results, while the solid line corresponds to the singular term $K_I/\sqrt{2\pi r}$, where r is the distance to the crack tip. For all values of uncracked ligament, the region of dominance of the stress intensity factor, as calculated with the assumptions of isotropy and homogeneity, is less than 1 μm (the average grain size). The lack of a well-developed K_I field renders the stress intensity factor an inappropriate direct crack tip-characterizing parameter for this specimen.

IV. RESULTS

A fractured sample is shown in the SEM micrograph in Fig. 8 and demonstrates that fracture is largely transgranular; this was true for all specimens, both doped and undoped. (The grain structure in the top surface in the undoped specimens was not as visible as that in Fig. 8, but the fracture path could still be discerned as transgranular.) It appears that the grain boundaries do not significantly weaken the structure.

The average critical value of the *J*-integral, $\overline{J}_c$, itself is shown in Table I. Significant out-of-plane deflections were observed when testing the 2.5 μm doped specimens; this and the nearly unphysical values of $\overline{J}_c$ [~80 times that of single crystal silicon (Table II) at a temperature far below the brittle-ductile transition] persuade us to discard these data. The remaining values range from 16 to 62 N/m. The relatively large standard deviations imply that either large uncertainties attend our determination of $\overline{J}_c$, in spite of the FEM calibrations
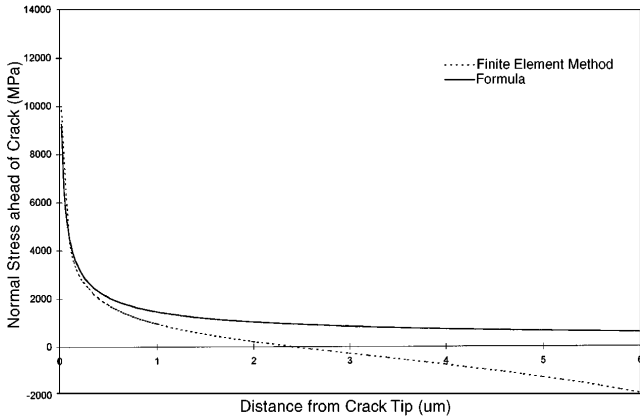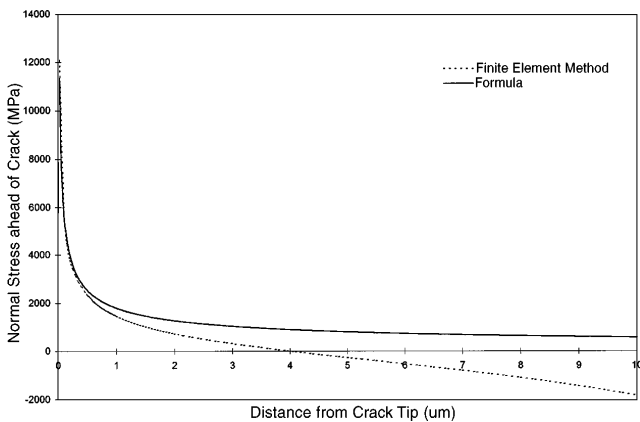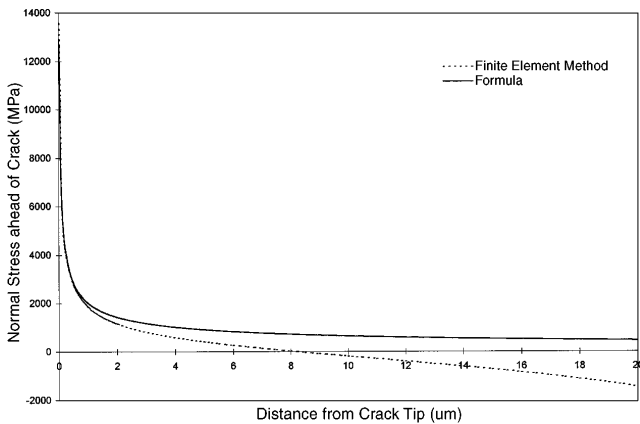
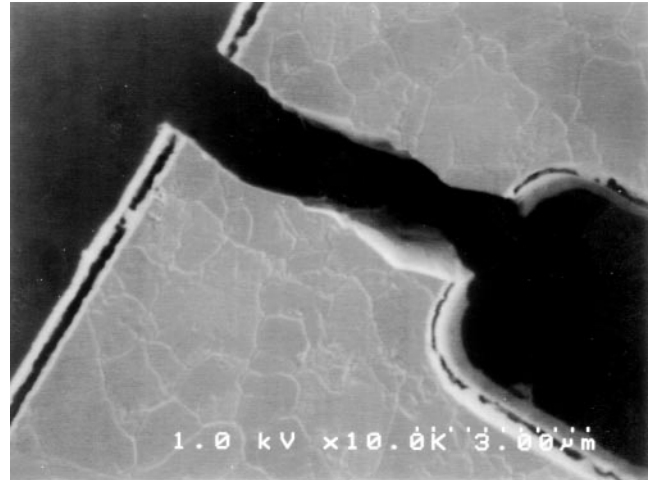FIG. 7. Normal stress distribution ahead of the crack: (a) $x = 6$ μm; (b) $x = 10$ μm; and (c) $x = 20$ μm.

FIG. 8. SEM micrograph of a fractured 6 μm ligament B-doped microdevice. The crack path is almost entirely transgranular.

TABLE II. Reported values for the fracture toughness, K_{Ic}, of single crystal silicon, and the corresponding energy release rates, J_c, values.

Ref.	K_{Ic} (MPa $\cdot$ m$^{1/2}$)	J_c *(N/m)
a	0.9	4.8
b	1.2**	8.6
c	0.9	4.8
d	0.9	4.8
e	0.7	2.9
f	1.2	8.6

$*J = \frac{(1-\nu^2)K_I^2}{E}$

**Lowest value reported by these authors.

a. C. St. John, Philos. Mag. **32**, 1193 (1975).

b. R. J. Myers and B. M. Hillberry, in Fracture 1977: Fourth International Conference on Fracture **3B**, 1001 (1977).

c. C. P. Chen and M. H. Leipold, Bull. Am. Ceram. Soc. **59**, 469 (1980).

d. S. Johansson, F. Ericson, and J-A. Schweitz, J. Appl. Phys. **65**, 122 (1989).

e. S. B. Brown, G. Povirk, and J. Connally, Proc. IEEE MEMS93 **99** (1993).

f. M. P. de Boer, H. Huang, J. C. Nelson, Z. P. Jiang, and W. W. Gerberich, in *Thin Films: Stresses and Mechanical Properties IV*, edited by P. H. Townsend, T. P. Weihs, J. E. Sanchez, Jr., and P. Børgesen (Mater. Res. Soc. Symp. Proc. **308**, Pittsburgh, PA, 1993), p. 647.

shown in Figs. 4 and 5, or that large fluctuations in the local resistance to crack growth at the notch tip are present. We incline to the latter view and tentatively conclude that neither the uncracked ligament length, the presence or absence of boron doping or Syton polishing, nor the film thickness affect $\overline{J}_c$.

The difference between single crystal fracture toughness and the present $\overline{J}_c$ data is large. A survey of the literature of single crystal fracture toughness data is shown in Table II; the $\overline{J}_c$ for single crystals ranges from 2.9 to 8.6 N/m. As mentioned in the introduction, the current samples may contain residual stresses,[5] which may affect the magnitude of $\overline{J}_c$. Furthermore, the non-planar crack path in Fig. 8 shows that some Mode II loading must be present, which will also affect the de-

rived value of $\overline{J}_c$. In brittle ceramics, similar differences between single crystal and polycrystalline toughnesses are in fact the rule, and are usually attributed to crack shielding due to residual stresses, crack bridging due to tortuous crack paths, and anisotropy in single crystal fracture toughness.[8] Which of these are relevant to the present data, or what other explanations pertain, await further study. Toward this end, we have made significant design changes in both the specimen geometry and the means of external loading of these microfracture mechanics specimens, in an attempt to provide more robust data. These data will be reported in the near future.

V. ADDENDUM

After writing this paper, we have learned that Sakata *et al.*[9] have measured the fracture toughness, K_{Ic}, of 2 μm thick polysilicon films of varying doping conditions and microstructures. Their measurements ranged from 2 to 4 MPa$\sqrt{\text{m}}$, corresponding to critical energy release rates of 20–90 N/m, in good agreement with our data.

REFERENCES

1. J. A. Connally and S. B. Brown, Science **256**, 1537 (1992).
2. L. S. Fan, R. T. Howe, and R. S. Muller, Sensors and Actuators **A21–A23**, 872 (1990).
3. F. Ericson and J. A. Schweitz, J. Appl. Phys. **68**, 5840 (1990).
4. S. Johansson, F. Ericson, and J. A. Schweitz, J. Appl. Phys. **65**, 122 (1989).
5. H. Kahn, S. Stemmer, K. Nandakumar, R. L. Mullen, R. Ballarini, M. A. Huff, and A. H. Heuer, IEEE Proc. 9th Annual Int. Workshop on Microelectromechanical Systems, San Diego, CA, 343 (1996).
6. T. I. Kamins and T. R. Cass, Thin Solid Films **16**, 147 (1973).
7. A. van der Drift, Philips Res. Repts. **22**, 267 (1967).
8. S. W. Freiman, Bull. Am. Ceram. Soc. **67** (2), 392 (1988).
9. J. Sakata, Toyota Central Research and Development Laboratories, Nagakute, Aichi 480-11, Japan, private communication, October 21, 1996.